Stability and sensitivity analysis of hydrodynamic instabilities in industrial swirled injection systems

Thomas Kaiser, Thierry Poinsot, Kilian Oberleithner

Thomas L. Kaiser[1]
Institut de Mécanique des Fluides de Toulouse,
UMR CNRS/INP-UPS 5502,
Toulouse 31400, France
e-mail: tkaiser@imft.fr

Thierry Poinsot
Institut de Mécanique des Fluides de Toulouse,
UMR CNRS/INP-UPS 5502,
Toulouse 31400, France

Kilian Oberleithner
Chair of Fluid Dynamics,
Technische Universität Berlin,
Berlin 10623, Germany

Stability and Sensitivity Analysis of Hydrodynamic Instabilities in Industrial Swirled Injection Systems

The hydrodynamic instability in an industrial, two-staged, counter-rotative, swirled injector of highly complex geometry is under investigation. Large eddy simulations (LES) show that the complicated and strongly nonparallel flow field in the injector is superimposed by a strong precessing vortex core (PVC). Mean flow fields of LES, validated by experimental particle image velocimetry (PIV) measurements, are used as input for both local and global linear stability analysis (LSA). It is shown that the origin of the instability is located at the exit plane of the primary injector. Mode shapes of both global and local LSA are compared to dynamic mode decomposition (DMD) based on LES snapshots, showing good agreement. The estimated frequencies for the instability are in good agreement with both the experiment and the simulation. Furthermore, the adjoint mode shapes retrieved by the global approach are used to find the best location for periodic forcing in order to control the PVC. [DOI: 10.1115/1.4038283]

1 Introduction

Swirled fuel injection systems are often used in modern combustion chambers. They provide enhanced mixing and fuel atomization and—in case the swirl is large enough to support vortex breakdown—flame anchoring in the central recirculation zone. In many cases, these flows are superimposed by a coherent hydrodynamic instability of azimuthal wave number $m = 1$, the precessing vortex core (PVC). Recent studies have shown that the PVC can interact with thermoacoustic instabilities [1,2] and in doing so may change the stability properties of a combustion system. Nevertheless, the PVC can lead to an increase of turbulence and therefore may improve mixing [3]. For these and other reasons, the PVC has increasingly been in the focus of research during the last years.

In recent years, linear stability analysis (LSA) of turbulent flows has been established as a well suited method to analyze the PVC. Two basically different methods to address LSA are the local stability analysis and the global stability analysis. In the former, the flow field is assumed to be parallel or only weakly nonparallel, and the analysis is performed sequentially on velocity profiles extracted at one axial position. Using this method, Lessen et al. [4] conducted one of the first analyses on swirling flows. They investigated the impact of swirl on the stability of the Batchelor vortex, a model for a trailing line vortex behind an air plane wing tip. The stability of weakly nonparallel flows was later on addressed by Chomaz et al. [5] and Pier et al. [6], who postulated frequency selection criteria for global modes in spatially developing flows. Gallaire et al. [7] showed that these criteria are capable of reproducing the precession frequency of a PVC occurring in a direct numerical simulation with reasonable accuracy. Furthermore, Oberleithner et al. [8] reproduced the frequency and the three-dimensional mode shape of the PVC occurring in their experiment using local stability analysis. Applying the same approach, Oberleithner et al. [9] showed that the flame roll-up caused by hydrodynamic instabilities correlates clearly with the flame describing function of a laboratory combustor.

Because of its higher computational costs, the approach of global stability analysis was for a long time out of scope until Pierrehumbert et al. [10] used two and three-dimensional global analysis to understand the instability mechanisms in a periodic row of vortices in 1982. Since then, the method has increasingly been used during the last decades. It is neither limited by the parallel flow assumption nor by any symmetry. Nowadays, applications range from academic test cases like cylinder wake flows [11] to the hole tone configuration explaining the mystery of the whizzing tea pot [12]. Adjoint methods based on global stability analysis give valuable insight into the internal feedback of hydrodynamic instability mechanisms. Juniper and Pier [13], for example, used structural sensitivity analysis to find the location of highest sensitivity to changes in the internal feedback mechanism of a confined co-flow wake and a cylinder wake, using both local and global stability analysis. Recently, Tammisola and Juniper [14] used global stability analysis on the mean flow in the interior of a fuel injector.

Both local and global approaches have been used extensively to understand the feedback mechanisms in the flow field of a PVC and yielded information for its control. However, despite its potential industrial relevance, most of the research conducted is focused on academic swirlers with—compared to industrial injection systems—strongly simplified geometries. This paper, therefore, addresses the following questions: What kind of linear stability approaches can be transferred from academical test cases to real industrial swirled injection systems of complex geometries and complicated mean flows and which information based on these methods is useful to control the coherent structures?

The fact that in most industrial injection systems, the flow is strongly nonparallel is supposed to be a major problem for the local stability analysis. On the other hand, most global stability codes use high order accurate discretization schemes to solve the governing equations, which only work on structured meshes, making an application to complex geometries difficult if not impossible. In this paper, the calculations using classical local stability

theory are compared to predictions based on a global stability code using triangular finite elements for unstructured meshes. The investigated geometry is an industrial, two-staged, counter-rotative, fuel injection system. LSA is based on the mean flow obtained from large eddy simulations (LES), which also provide the mode shapes and frequencies of the PVC. The predicted wave maker location, meaning the origin of the perturbation, and the mode shapes are compared for the local and global approach.

Section 2 deals with the theory of both global and local LSA. Section 3 explains the simulation setup and the LES performed. Sections 4.1 and 4.2 show and discuss the results of global and local stability analysis, respectively, and Sec. 5 summarizes the results.

2 Linear Stability Analysis Theory and Numerical Discretization

In order to receive the governing equations for LSA, the pressure and velocity components in the Navier–Stokes equations are decomposed using the triple decomposition

$$\varphi = \overline{\varphi} + \tilde{\varphi} + \varphi' \tag{1}$$

where $\overline{\varphi}$ denotes the mean part, $\tilde{\varphi}$, the coherent fluctuation, and φ', the stochastic fluctuation. After some rearrangements, one arrives at the following set of equations for the coherent part [15]:

$$\frac{\partial \tilde{u}_i}{\partial x_i} = 0 \tag{2a}$$

$$\frac{\partial \tilde{u}_i}{\partial t} + \overline{u}_j \frac{\partial \tilde{u}_i}{\partial x_j} + \tilde{u}_j \frac{\partial \overline{u}_i}{\partial x_j} = -\frac{\partial p}{\partial x_i} + \frac{1}{\mathrm{Re}} \frac{\partial^2 \tilde{u}_i}{\partial x_j \partial x_j} + \frac{\partial}{\partial x_j}\left(\overline{\tilde{u}_i \tilde{u}_j} - \tilde{u}_i \tilde{u}_j\right) - \frac{\partial}{\partial x_j}\left(\langle u_i' u_j' \rangle - \overline{u_i' u_j'}\right) \tag{2b}$$

Here, u_i is the velocity while x and t stand for the spatial coordinate and time, respectively. The indices i and j are to be treated according to the Einstein notation. The variable Re is the Reynolds number

$$\mathrm{Re} = \frac{UD}{\nu} \tag{3}$$

where U and D are the arbitrary velocity and length scales used to nondimensionalize the equations. The values used in the framework of this paper are $D = 4.2$ mm and $U = 50$ m/s. Due to the linear framework, the third term in Eq. (2b) vanishes. The fourth term, however, describes the stochastic–coherent interaction and can be of first-order in turbulent flows. As these terms are a priori unknown, the set of equations has to be closed.

The approach of modeling the stochastic–coherent interaction with an additional eddy viscosity is frequently used in LSA [14,16]. This paper follows this strategy and derives the eddy viscosity based on the Boussinesq approximation, which relates the mean flow strain rates to the stochastic fluctuations. Since the approach yields an eddy viscosity for every independent combination in the product of the stochastic velocity fluctuation components, $u_i' u_j'$, their least mean square is used [17], yielding

$$\nu_\mathrm{e} = \frac{\left(-\overline{u_i' u_j'} + \frac{2}{3} K \delta_{ij}\right) \cdot \left(\frac{\partial \overline{u}_j}{\partial x_i} + \frac{\partial \overline{u}_i}{\partial x_j}\right)}{\left(\frac{\partial \overline{u}_k}{\partial x_l} + \frac{\partial \overline{u}_l}{\partial x_k}\right) \cdot \left(\frac{\partial \overline{u}_k}{\partial x_l} + \frac{\partial \overline{u}_l}{\partial x_k}\right)} \tag{4}$$

where K is the turbulent kinetic energy and δ is the Kronecker delta. Due to the spatial filtering of turbulence performed in LES, the highest frequencies of the turbulent spectrum are not resolved. This results in a slightly decreased eddy viscosity in comparison with a fully resolved simulation or an experiment. In the framework of this paper, it is assumed that the LES subgrid-scale turbulent viscosity, ν_t, accounts for this difference. Adding the molecular, ν_m, and the resolved eddy viscosity, ν_e, then leads to a total viscosity of

$$\nu_\mathrm{tot} = \nu_\mathrm{m} + \nu_\mathrm{e} + \nu_\mathrm{t} \tag{5}$$

2.1 Global Stability Analysis. According to the terminology suggested by Theofilis [18], TriGlobal stability analysis is performed in a three-dimensional domain where all three directions are inhomogeneous. BiGlobal stability analysis is also performed in the three-dimensional domain, where one direction is assumed to be homogeneous. The swirling flow considered in this work is axisymmetric and a BiGlobal approach is sufficient. For convenience, cylindrical coordinates are used to formulate the conservation equations. In order to arrive at the governing equations for BiGlobal stability in axisymmetric flows, the following modal approach is inserted into Eq. (2):

$$\{\tilde{u}_r, \tilde{u}_\theta, \tilde{u}_x, \tilde{p}\} = \{F(x,r), G(x,r), H(x,r), \Pi(x,r)\} \exp(im\theta - i\omega t) \tag{6}$$

In the BiGlobal approach, the eigenfunctions F, G, H, and Π are dependent on both the radial and axial coordinates. The azimuthal wave number, m, accounts for the azimuthal periodicity, while ω is the complex-valued frequency. Its imaginary part, ω_i, corresponds to the temporal growth rate and its real part, ω_r, stands for the harmonic frequency in time. The resulting set of equations can be formulated as an eigenvalue problem of ω

$$\mathbf{A}\Phi = \omega \mathbf{B}\Phi \tag{7}$$

with the eigenvector

$$\Phi = [F(x,r), G(x,r), H(x,r), \Pi(x,r)]^\mathrm{T} \tag{8}$$

and the eigenvalue ω. The eigenvalue problem is discretized using FREEFEM++ [19], an open source software tool solving differential equations. It performs the finite element method on triangle-shaped elements in two dimensions and on tetraeders in three-dimensional domains. For the solution of the eigenvalue problem, the software package ARPACK [20] is used. The shape functions used to discretize the governing equations are of second-order for the velocity components and of first-order for the pressure. The code was successfully validated against the code of Paredes et al. [21] on the configuration of Rukes et al. [16]. The conditions applied at the domain boundaries are listed in Table 1. For every pair of right eigenvalue and eigenvector, (ω, Φ) there exists a pair of left—or adjoint—eigenvalue and eigenvector, ($\omega^\dagger$, $\Phi^\dagger$), where $\omega^\dagger$ is the complex conjugate of ω. While the right eigenvector corresponds to the mode shape of the instability, the left eigenvector

Table 1 Boundary conditions for the perturbations *F*, *G*, *H* and Π for both local and global stability analysis; *n* is the normal vector of the boundary

Walls	Inlets/outlets	Axis global	Axis local
$F = 0$	$F = 0$	$\frac{\partial F}{\partial r} = 0$	$F + G = 0$
$G = 0$	$G = 0$	$\frac{\partial G}{\partial r} = 0$	$2\frac{\partial F}{\partial r} + \frac{\partial G}{\partial r} = 0$
$H = 0$	$H = 0$	$H = 0$	$H = 0$
$\frac{\partial \Pi}{\partial n} = 0$	$P = 0$	$\frac{\partial \Pi}{\partial r} = 0$	$P = 0$

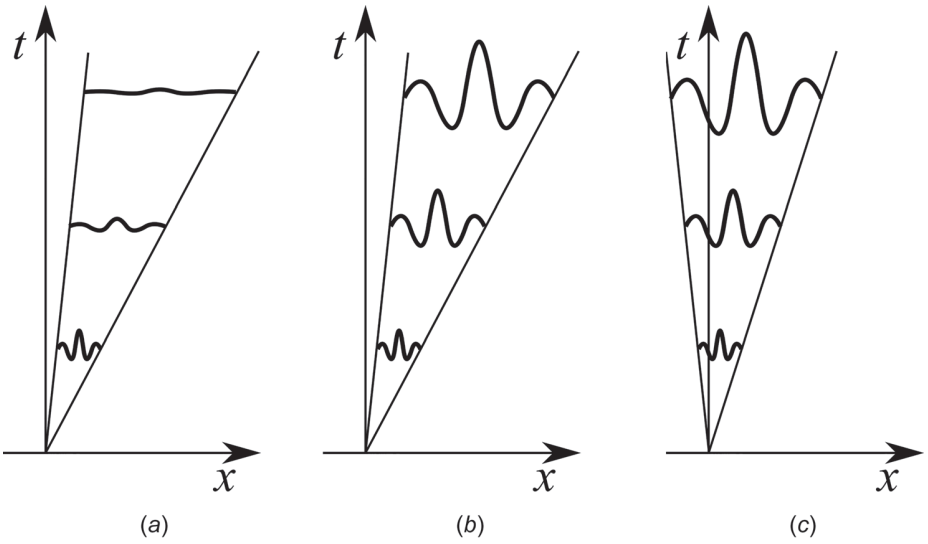

Fig. 1 Schematic representations of wave packets in flows with different stability properties: (*a*) stable flow, (*b*) convectively unstable flow, and (*c*) absolutely unstable flow

shows the receptivity of the mode to periodic forcing. In this context, Giannetti and Luchini [22] investigate the feedback mechanism involving the corresponding left and right eigenvectors. They define the structural sensitivity as the normalized product of both eigenvectors

$$\lambda(x,r) = \frac{||\Phi^\dagger||\,||\Phi||}{\int \Phi^\dagger \cdot \Phi dS} \tag{9}$$

The global approach is especially interesting for complex geometries since no parallel flow assumption is made like in the local analysis. However, care has to be taken regarding the boundary conditions. The boundaries have to be chosen far away from the wave maker in order to not influence the mode shapes.

2.2 Local Stability Analysis. For the local analysis, a quasi-parallel mean flow is assumed. Now, the perturbation is periodic in axial and azimuthal direction, reading

$$\{\tilde{u}_r, \tilde{u}_\theta, \tilde{u}_x, \tilde{p}\} = \{iF(r), G(r), H(r), \Pi(r)\} \exp(im\theta + i\alpha x - i\omega t) \tag{10}$$

where α is the axial wave number. Note that the eigenfunctions unlike in Eq. (7) only depend on the radial coordinate. The real part of α is the axial wave number and its imaginary part corresponds to the negative of the spatial growth rate. When inserting Eq. (10) in Eq. (2), the governing equations for the local stability analysis yield a dispersion relation for α and ω, which can be described as an eigenvalue problem. For its solution, the Chebyshev collocation technique has proven to be a highly efficient discretization method [23] and is therefore used in the framework of this paper. The boundary conditions applied are listed in Table 1. The properties of the eigenvalue problem depend on the type of analysis:

(1) Temporal analysis. The axial wave number, α, is fixed to a real value and the eigenvalue problem is solved for a complex ω

$$\mathbf{A}(\alpha_r)\Phi = \omega \mathbf{B}(\alpha_r)\Phi \tag{11}$$

(2) Spatial analysis. The frequency, ω, is fixed to a real value and the eigenvalue problem is solved for a complex α. The eigenvalue problem in the spatial analysis is quadratic in α. One way to solve the problem is to add additional unknowns and thereby linearize the problem. The generalized eigenvalue problem then becomes

$$\mathbf{A}(\omega_r)\Phi = \alpha \mathbf{B}(\omega_r)\Phi \tag{12}$$

Unlike in a temporal analysis, where a perturbation can only move in t^+-direction and never in t^--direction, a perturbation in space can evolve in both x-directions. Without further information, it therefore is a priori unclear whether the pair of α and Φ belongs to an α^+-branch or an α^--branch.

(3) Spatiotemporal analysis: Here, both α and ω are complex valued and either Eq. (11) or Eq. (12) is solved.

Figures 1(*a*)–1(*c*) schematically show the evolution of a wave packet in space and time for flows with different stability properties. The flow is called *stable* when all perturbations decay in time in every Galilean reference frame (Fig. 1(*a*)). In *convectively unstable* flows, perturbations grow in time but are convected away from their source, leaving the base flow undisturbed for $t \to \infty$. *Absolutely unstable* flows give rise to oscillations, which contaminate the entire flow for $t \to \infty$.

To distinguish between convectively unstable and absolutely unstable flows, a spatiotemporal analysis has to be performed in order to examine the group velocity, which is defined as

$$c = \frac{\partial \omega}{\partial \alpha} \tag{13}$$

An absolutely unstable flow must give rise to an instability wave with positive temporal growth rate and zero group velocity. A perturbation moving at zero group velocity is marked by a saddle point of ω in the complex α-plane

$$c(\alpha_0) = \frac{\partial \omega}{\partial \alpha}(\alpha_0) = 0 \tag{14}$$

The related frequency at the saddle point is called the *absolute frequency*, ω_0. If its imaginary part, $\omega_{0,i}$, is larger than zero, then the base flow profile is absolutely unstable. In a spatially developing flow, a region of absolute instability is a necessary condition for a global mode [24]. According to Chomaz et al. [5], the frequency

of the global mode is defined by the value of the absolute frequency at the saddle point in the complex X-plane

$$\frac{\partial \omega_0}{\partial X}(X_s) = 0 \tag{15}$$

and the frequency of the global mode is

$$\omega_g = \omega_0(X_s) \tag{16}$$

The origin of the global mode, the so-called wavemaker, is determined by the switch between the α^+- and α^--branches [25,26].

To summarize, the methodology to find and reconstruct the global mode using local stability analysis consists of four steps. In the first step, ω_0 and α_0 are determined by finding the saddle point in the complex α-plane. To do so, a temporal analysis is performed at arbitrary axial positions in the flow for various fixed α until a physical branch with positive temporal growth rate for a finite range of α is found. Thereafter, the resulting curve is extended to the complex α-plane by performing a spatiotemporal analysis. Then, in the complex α-plane, the saddle point of the dispersion relation is found. In the second step, the saddle point is tracked while sweeping through the mean flow in axial direction. The flow is absolutely unstable in regions where the imaginary part of the absolute frequency is larger zero. Then, the complex frequency as a function of the axial position is fitted by Padé polynomials and extended to the complex X-plane and the saddle point X_s is found. According to Eq. (16), the corresponding frequency is the global frequency. In the third step, a spatiotemporal analysis is performed at the complex frequency of ω_g for all the axial positions of interest and the α^+ and α^- branches and the wave maker location are identified. In the fourth step, the global mode shape can be reconstructed by applying

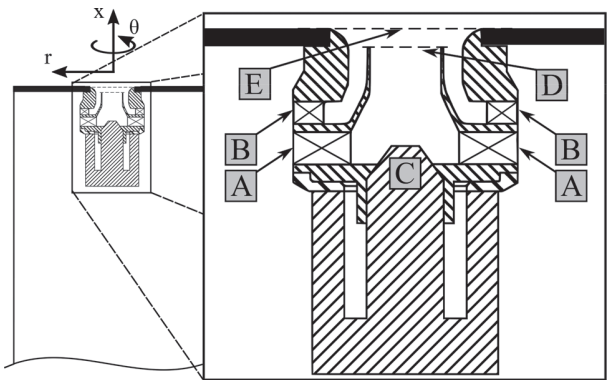

Fig. 2 Schematic sketch of the experiment: (*a*) primary vanes, (*b*) secondary vanes, (*c*) center body, (*d*) primary injector exit plane, and (*e*) dump plane

$$\{u_r, u_\theta, u_x, p\} = \Re\left\{\{iF, G, H, \Pi\}\exp\left(\mathrm{im}\theta + i\int_{x_0}^{x} \alpha x\, dx - i\omega t\right)\right\} \tag{17}$$

where the F, G, H, and Π are the normalized eigenfunctions. In Eq. (17), α corresponds to the α^- branch upstream of the wave maker location, and to α^+ downstream of the wave maker.

3 Experiment and Simulations

In this section, the experimental and numerical setups are outlined and the mean flows are discussed, which serve as the base flow for the LSA.

3.1 Experimental Setup. Figure 2 shows details of the experimental setup. The swirl injection system is inserted at the exit of a plenum of diameter 82 mm and length of 590 mm and blows into the atmosphere. The swirler consists of two passages: The primary air stream flows in the inner region through eight tangential vanes, whereas the secondary flow enters the external region through eight tangential vanes in counter-rotative flow direction with respect to the primary stream.

Flow-field measurements are carried out using particle image velocimetry (PIV) in order to validate the LES computations. A $20 \times 32\,\mathrm{mm}^2$ region of interest is selected in a longitudinal plane. Particular attention is paid to capture the velocity profiles as close as possible to the dump plane: First, the laser sheet is thickened to 1 mm to reduce the out-of-plane displacements of the seeding particles. Furthermore, based on a parametric study, the time delay between the pulses is set to 4 μs.

In addition to PIV measurements, far-field pressure fluctuations are measured with a microphone placed at $x = 0$ and $r = 300$ mm (not shown in Fig. 2). For the operating point of a mass flow rate of $\dot{m} = 4.29\,g/s$ at atmospheric conditions, the sound pressure spectrum in Fig. 3 shows three distinct peaks at approximately $f = 700$ Hz, 3150 Hz, and 6300 Hz. However, proper orthogonal decomposition of the PIV snapshots did not reveal any coherent structures.

3.2 LES Setup. The LES are performed using the AVBP code [27], which is specialized in solving the compressible Navier–Stokes equations on unstructured grids (developed at Centre Européen de Recherche et de Formation Avancée en Calcul Scientifique (CERFACS) and Institute Français du Pétrole-Énergies nouvelles (IFPEN)). For discretization, the two-step Taylor–Galerkin 'C' scheme [28] is used, which is third-order accurate in space and time. Subgrid turbulence is modeled with the sigma model [29]. The computational domain comprises the last 90 mm of the upstream plenum, the swirler, and a half sphere modeling the atmosphere. In total, it is discretized with 10.86×10^6 cells. The edge length of the finest cells is 45 μm. The time-step is fixed to $\Delta t = 3.3 \times 10^{-8}$ s, which resembles approximately a maximal Courant–Friedrichs–Lewy number of 0.9. The velocity profile at the inlet is imposed according to hot-wire anemometry.

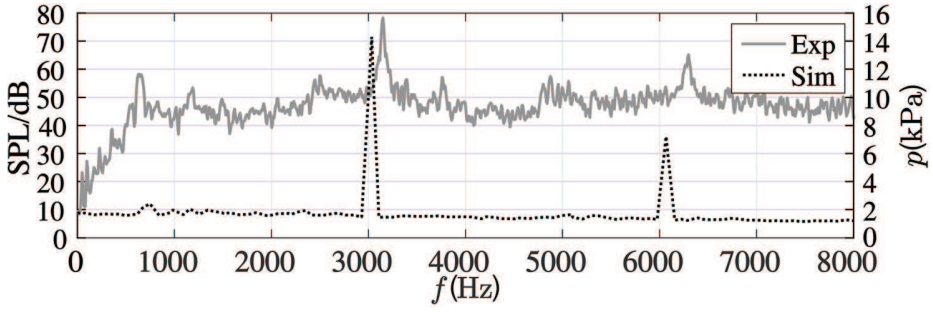

Fig. 3 Experimental sound pressure level and dynamic mode decomposition (DMD) spectrum of pressure based on LES snapshots

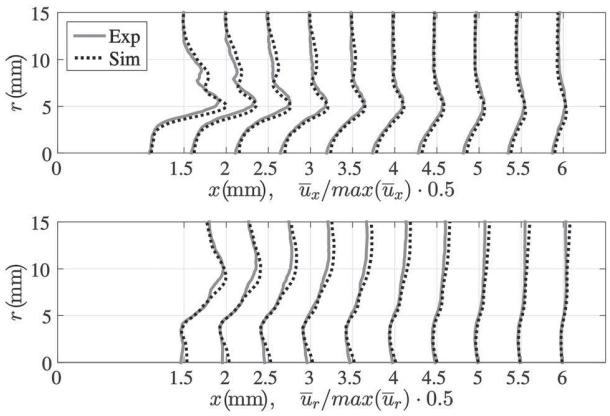

Fig. 4 Comparison of experimental and LES mean profiles of axial velocity, $\overline{u}_x$, and radial velocity, $\overline{u}_r$, for varying axial positions

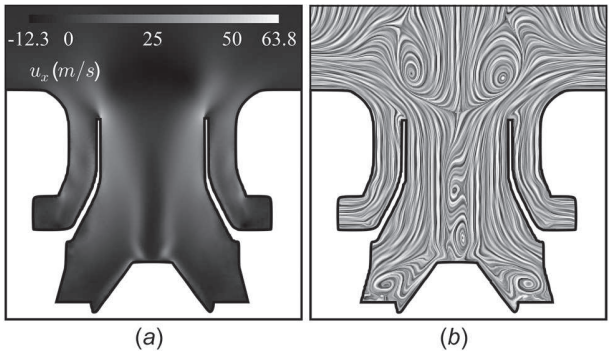

Fig. 5 Mean flow field inside the injector: (*a*) axial velocity and (*b*) 2D line integral convolution

In Fig. 4, the LES is validated against the experimental axial and radial mean flow components downstream of the swirler. The plot shows good agreement for both the axial and the radial velocity components.

3.3 Mean Flow and Coherent Structures Based on LES. The LES-based mean axial velocity and the mean flow stream lines in axial and radial directions are shown in Fig. 5. Because of the strong swirl in the primary injector, most of the fluid is transported close to the primary injector walls, while in the core axial velocities are low and partially negative. At the edge of the center body, a thin ring of high velocity occurs, which can be seen in the axial component in Fig. 5(*a*). This causes strong shear layers in this region. After a convergent and a parallel section, the primary stage opens to the secondary stage. Directly downstream of the injector, the streamlines are deflected perpendicular to the injector axis. Therefore, the recirculation zone does not close, and gas from the atmosphere is sucked in and deflected with the fluid from the injector perpendicular to the swirler axis. Figure 5 demonstrates that the flow is strongly nonparallel, especially outside of the primary injector.

A DMD [30], a decomposition method relating a frequency to every mode, is performed based on LES snapshots. The resulting DMD spectrum is displayed in Fig. 3 by the dotted line. It shows distinct peaks that are in good agreement with the experimental pressure spectrum. The method shows that the peak at approximately 700 Hz is related to an axisymmetric fluctuation, which will not be further investigated in this paper. The second very distinctive peak at $f = 3030$ Hz in the DMD spectrum is related to a PVC of azimuthal wave number $m = 1$. The PVC is accompanied by several higher harmonics of which only the first one is visible at $f = 6060$ Hz in Fig. 3. The focus of this paper, however, shall be on the dominating instability. The left column in Fig. 6 shows the DMD mode shapes of the PVC of azimuthal wave number $m = 1$. The fact that the maximum of the coherent structure is close to the exit plane of the primary injector and that it decays rapidly thereafter explains why PIV measurements could not capture the instability since visual access in the interior of the swirler is not possible.

4 Results

As demonstrated above, the LES captures the mean flow and the PVC dynamics sufficiently accurate. For this reason, the LSA is based on the LES mean fields and the stability eigenmodes are validated with the DMD modes extracted from the LES. In the following, the results of the global and local approach will be discussed.

4.1 Results From the Global Stability Analysis. Compared to local stability analysis, the procedure of global stability analysis is relatively straightforward since no frequency selection criteria, complex mapping, or global reconstruction from local data is necessary.

Figure 7 illustrates the global spectrum of the considered configuration. It demonstrates that all modes are stable except one single mode at $\omega_g \approx 1.89 + 0.01i$, which is slightly unstable. The fact that the growth rate is almost equal to zero is in line with the expectations of LSA based on a temporally averaged flow. Since the instability is at its limit cycle, it neither grows nor decays. Global stability analysis overestimates the frequency of the PVC by about 18%. Figure 6 compares the global mode shapes in the third row to the corresponding DMD modes in the first row. The predicted axial velocity and pressure fluctuations agree very well with the DMD modes although the fluctuations decay to rapidly upstream of their maximum amplitude. This is very likely due to the low-order numerical discretization scheme used. Another global stability code [21] with a high-order dispersion relation conserving discretization schemes showed better results in this region. Although, outside the primary injector the agreement of the mode shapes is satisfactory for the radial and the azimuthal velocities, they do not match close to the exit plane of the primary injector.

Figure 6 shows the corresponding adjoint modes in the fourth column indicating that the hydrodynamic instability is by far most receptive to azimuthal forcing at the intersection between the vanes and the primary injector. The radial and azimuthal velocities of the adjoint mode show a distinct peak in this region. The maxima of the axial velocity and pressure are both located at the exit plane of the primary injector. The adjoint modes show that at first-order the most efficient and practical way to force or control the PVC is to pulse directly the flow through the vanes periodically. By doing so, both the azimuthal and the radial velocity components are excited at their most receptive positions. The maximum of the adjoint mode's axial velocity is far from any wall, which makes an actuation by air injection practically difficult at this position. Finally, Fig. 8(*a*) shows that the structural sensitivity, and therefore the location of strongest feedback, is close to the exit plane of the primary injector.

4.2 Results From the Local Stability Analysis. The methodology laid out in Sec. 2 is followed during the local stability analysis. The first step is related to finding the position of the saddle point of the complex frequency, ω, in the complex α-plane. The real and imaginary parts of ω as a function of the complex α are exemplary shown in Fig. 9 for the exit plane of the primary injector. The pair of frequency and wave number for which

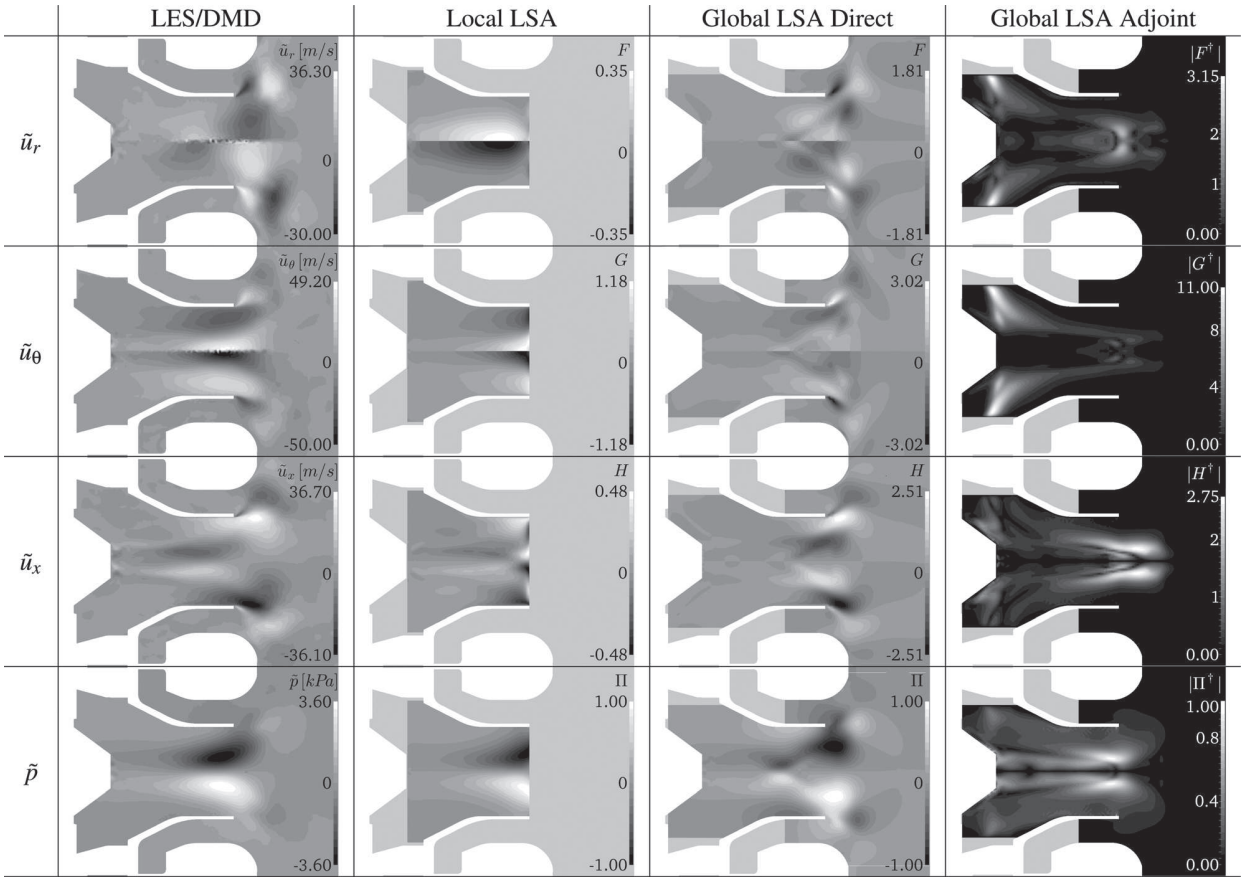

Fig. 6 PVC modes based on LES/DMD and LSA; right column: global LSA adjoint modes

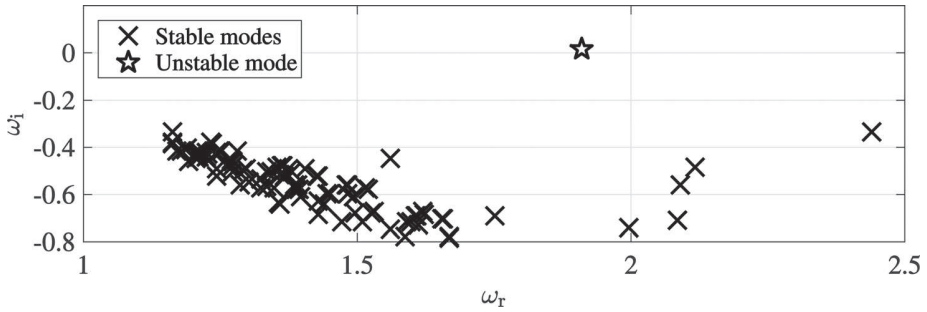

Fig. 7 Spectrum of global stability analysis

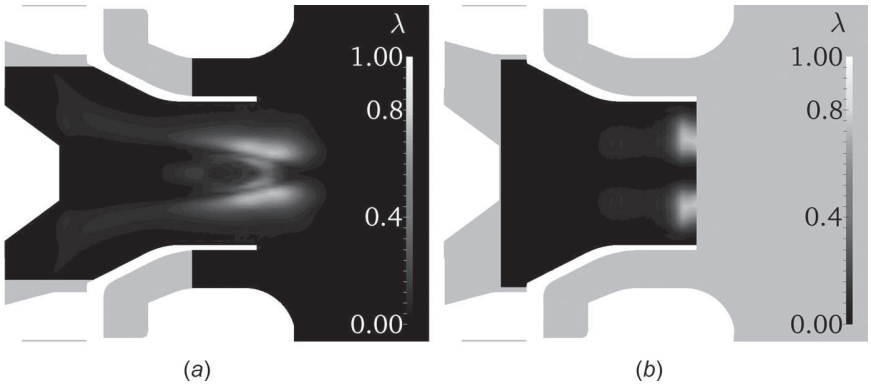

Fig. 8 Structural sensitivity, λ: (*a*) global LSA and (*b*) local LSA

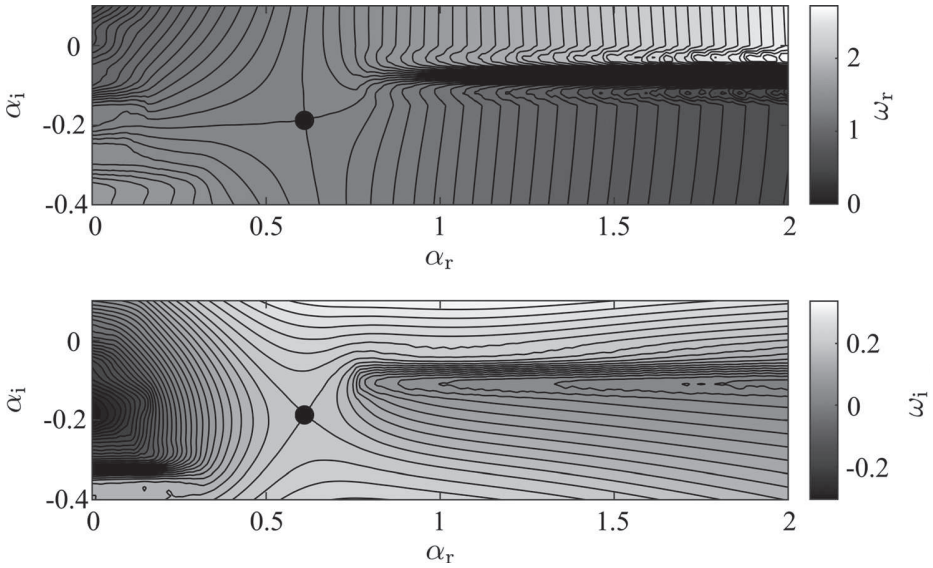

Fig. 9 Real and imaginary part of the nondimensional frequency, ω, in the complex α-plane for the velocity profile at the exit of the primary injector

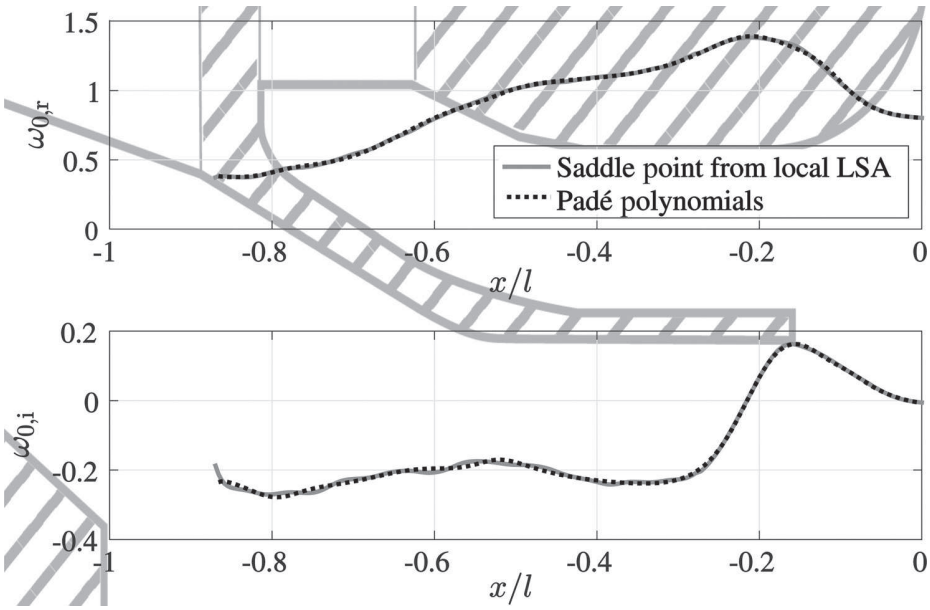

Fig. 10 Real and imaginary part of the absolute frequency, ω_0, over the axial coordinate, *x*

Eq. (14) is satisfied for the 1D velocity profile under investigation is $\omega = 1.36 + 0.20i$ and $\alpha = 0.61 - 0.19i$. Since the imaginary part at the saddle point is positive, the flow is absolutely unstable at this position. According to the second step of the methodology, the saddle point has to be tracked in positive and negative x-direction. The resulting curves of the complex absolute frequency as a function of the axial position are shown in Fig. 10. In this plot, the axial coordinate is indicated by the schematic of the swirler in the background. The flow is absolutely unstable in the region between $x = -0.22l$ and $x = 0l$. The peak of the $\omega_{0,i}$ is close to the exit plane of the primary injector. The graph is consequentially extruded in the complex X-plane by the use of Padé polynomials. The result is visualized in Fig. 11. The plot of the complex frequency in the complex X-plane exposes a saddle point with the complex frequency $\omega = 1.33 + 0.16i$. According to Eq. (16), this is the frequency of the global mode. The error in comparison with the result in the LES is 17% and for a strongly nonparallel flow, reasonably accurate. The observation that the growth rates of the local approach are higher than of the global stability analysis is in line with the work of Juniper et al. [31], who investigated the influence of confinement on the stability of wakes using both methods. They found that local stability analysis tends to slightly overestimate the growth rates.

In the third step, the wave maker location is found by detecting the branch switching between the α^+ and α^- branches. Figure 12 shows that the branch switching takes place directly at the exit plane of the primary injector. Starting from the base of the center body, the growth rate of the α^- branch is positive until the wave maker position. From this point on, the α^+ branch is followed, which indicates that for values of $x \geq -0.16\,l$, the mode decays in axial direction. Finally, after the global frequency and the wave maker location are determined, the mode shapes of the global

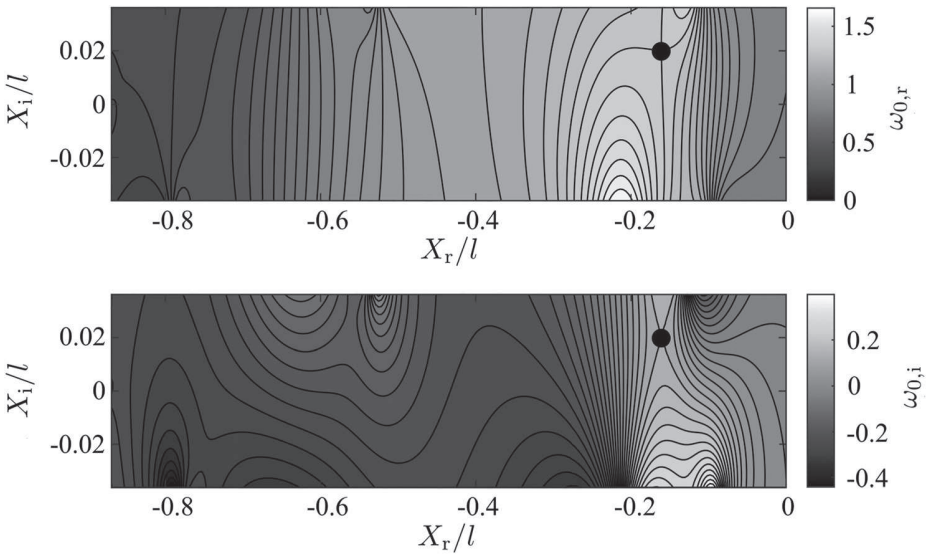

Fig. 11 Expansion of the absolute frequency, ω_0, into the complex *x*-plane

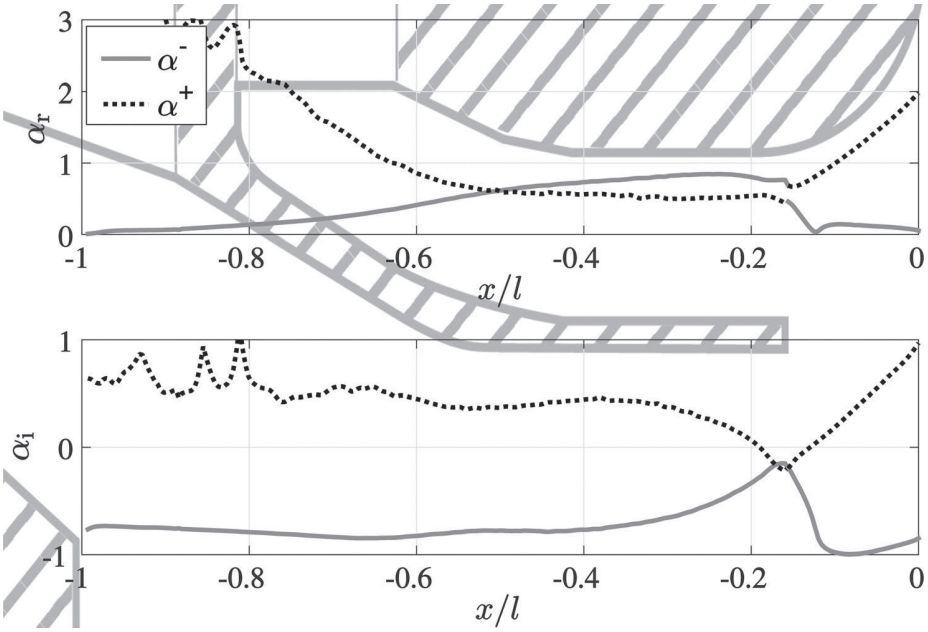

Fig. 12 α^+ and α^- as a function of the axial position

mode can be reproduced from a spatial analysis according to Eq. (17). Since the flow outside of the primary injector is highly nonparallel, the mode reconstruction is only performed within the primary injector. Figure 6 compares the reconstructed global modes in the second column to the DMD modes in the first column, which are based on the LES. The mode shapes show very good agreement in the radial and azimuthal velocity component and pressure. Some discrepancies can be seen in the axial component, close to the exit plane of the primary injector. It is interesting to note that the shear layers downstream of the central bluff body in the primary injector are excited by the perturbation and that this is captured by the local stability analysis, which is best visible in the axial component. Figure 8(*b*) shows the structural sensitivity based on the local stability analysis where the global adjoint modes were reconstructed from the local analysis data according to Ref. [13]. Like in the global analysis, the region of highest structural sensitivity is located at the exit of the primary injector.

5 Conclusion

The flow field in an industrial, swirled, two-staged fuel injection system of high geometrical complexity is investigated by LES, as well as local and global LSA. The aim of this study is to investigate the capability of local and global stability analysis to predict the dominant coherent structures and to reveal their origin and controllability based on adjoint methods.

Large eddy simulation is first compared to PIV measurements showing good agreement regarding the mean fields. The DMD of the LES data reveals a PVC of azimuthal wave number $m = 1$ dominating the flow dynamics inside the injector with its oscillation frequency matching the pressure oscillations measured in the

Table 2 PVC frequency and growth rates from the experiment, LES and global and local stability analysis; LES errors are based on the experimental value, while LSA errors are with respect to the LES. Errors of growth rates are calculated based on the frequency of the oscillation.

	Exp.	Sim.	Global	Local
Nondim. frequency ω_r	1.66	1.60	1.89	1.33
Nondim. growth rate ω_i	0	0	0.01	0.16
Error $\epsilon(\omega_\mathrm{r})$	—	−3.2%	+18%	−17%
Error $\epsilon(\omega_\mathrm{i})$	—	0	+0.6%	+10%

experiment. Linear hydrodynamic stability analysis is conducted based on the LES mean fields. The results from a local quasi-parallel stability analysis are compared to the results from a global stability analysis. Both approaches show that the wave maker region for the PVC is at the exit plane of the primary injector. The mode shapes in the primary injector are reconstructed from local LSA and compared to DMD modes derived from the LES snapshots. Despite the strong violation of the parallel flow assumption of local stability analysis, the agreement between this approach and DMD is satisfactory. Also, the estimated frequency is with an error of approximately 17% compared to LES reasonably accurate. The temporal growth rate is slightly overestimated by the local approach. The global approach, which is not restricted by the parallel flow assumption, is applied to the entire flow field inside and outside the injector. Outside the injector, the mode structure is very well reproduced, while inside the injector, the radial and azimuthal velocity components show discrepancies. The frequency estimated by the global approach is satisfactorily reproduced with an error of approximately 18%. The growth rate is close to zero, which is expected for a LSA based on a mean flow. The frequencies of the PVC in the experiment, the LES, and both in global and local stability analysis are concluded in Table 2 together with their corresponding errors. Furthermore, the global adjoint modes show that in a linear framework, the perturbation is most sensitive to azimuthal forcing at the vanes of the primary injector. Based on these results, the best way to control the PVC is to directly force the flow at the primary injector vanes.

Even though the flow field is already strongly nonparallel in the primary injector, the local analysis still provides unexpectedly well results in this region of the configuration. This leads to the conclusion that local stability analysis is in general applicable to hydrodynamic instabilities in complex geometries. On the other hand, the results show also the limit of this approach. Outside of the primary injector and especially in the free stream field, the flow is nonparallel in such an extent that the approach fails. As the global approach is not restricted by the nonparallel assumption, this method can be used in all kinds of geometries and flow fields. However, with the global approach, other difficulties emerge. As mentioned in the introduction, some solvers count on high-order accurate discretization schemes but by doing so are restricted to Cartesian meshes. An application to complicated geometries is therefore difficult or impossible. Using unstructured grids on the other hand simplifies the meshing considerably; however, the advantage of high-order accuracy is not given. In order to solve this problem, effort has to be paid on the improvement of the discretization schemes for unstructured meshes. Furthermore, a TriGlobal analysis might help to understand the discrepancies, which occur for the radial and the azimuthal components between the BiGlobal mode shapes and the LES.

Acknowledgment

The authors would like to express their gratitude toward Professor David Fabre and Lokman Bennani at Institute de Mécanique des Fluides Toulouse for very fruitful discussions on global stability analysis as well as Pradip Xavier for conducting the PIV measurements. Furthermore, the authors thank Pedro Paredes for providing his high-order global stability tool as a validation for our code as well as Jens Müller from TU Berlin for its application. Finally, the help of Laura Lacassagne, Thibault Bridel-Bertomeu and Guillaume Daviller—all at CERFACS—is hereby gratefully acknowledged.

This work was granted access to the high-performance computing resources of CINES under the allocation x20152b7036 made by Grand Equipement National de Calcul Intensif.

Funding Data

- European Research Council under the European Union's Seventh Framework Programme (FP/2007-2013)/ERC (Grant No. ERC-AdG 319067-INTECOCIS).
- Grand Equipement National de Calcul Intensif (Grant No. x20152b7036).

Nomenclature

c = group velocity
D = characteristic length scale
F = eigenfunction of radial velocity
G = eigenfunction of azimuthal velocity
H = eigenfunction of axial velocity
$i = \sqrt{-1}$
K = turbulent kinetic energy
m = azimuthal wave number
n = normal vector
p = pressure
r = radial coordinate
Re = Reynolds number
t = time
u = velocity
U = characteristic velocity
x = axial coordinate
X = complex x-axis

Greek Symbols

α = complex axial wave number
θ = azimuthal coordinate
λ = structural sensitivity
ν = viscosity
Π = eigenfunction of pressure
Φ = eigenvector
ω = complex angular frequency

Subscripts

$\langle\cdot\rangle_\mathrm{e}$ = eddy
$\langle\cdot\rangle_\mathrm{g}$ = global mode
$\langle\cdot\rangle_\mathrm{i}$ = imaginary
$\langle\cdot\rangle_\mathrm{m}$ = molecular
$\langle\cdot\rangle_r$ = radial component
$\langle\cdot\rangle_\mathrm{r}$ = real
$\langle\cdot\rangle_\mathrm{s}$ = saddle point
$\langle\cdot\rangle_\mathrm{t}$ = turbulent
$\langle\cdot\rangle_\mathrm{tot}$ = total
$\langle\cdot\rangle_x$ = axial component
$\langle\cdot\rangle_\theta$ = azimuthal component
$\langle\cdot\rangle_0$ = zero group velocity

Superscripts

$\langle\cdot\rangle^\dagger$ = adjoint
$\widetilde{\langle\cdot\rangle}$ = coherent fluctuation
$\overline{\langle\cdot\rangle}$ = mean
$\langle\cdot\rangle'$ = stochastic fluctuation
$\dot{\langle\cdot\rangle}$ = time derivative

References

[1] Ghani, A., Poinsot, T., Gicquel, L. Y., and Müller, J. D., 2016, "LES Study of Transverse Acoustic Instabilities in a Swirled Kerosene/Air Combustion Chamber," Flow, Turbul. Combust., **96**(1), pp. 207–226.

[2] Moeck, J. P., Bourgouin, J.-F., Durox, D., Schuller, T., and Candel, S., 2012, "Nonlinear Interaction Between a Precessing Vortex Core and Acoustic Oscillations in a Turbulent Swirling Flame," Combust. Flame, **159**(8), pp. 2650–2668.

[3] Stöhr, M., Boxx, I., Carter, C. D., and Meier, W., 2012, "Experimental Study of Vortex-Flame Interaction in a Gas Turbine Model Combustor," Combust. Flame, **159**(8), pp. 2636–2649.

[4] Lessen, M., Singh, P. J., and Paillet, F., 1974, "The Stability of a Trailing Line Vortex—Part 1: Inviscid Theory," J. Fluid Mech., **63**(4), pp. 753–763.

[5] Chomaz, J.-M., Huerre, P., and Redekopp, L. G., 1991, "A Frequency Selection Criterion in Spatially Developing Flows," Stud. Appl. Math., **84**(2), pp. 119–144.

[6] Pier, B., Huerre, P., and Chomaz, J.-M., 2001, "Bifurcation to Fully Nonlinear Synchronized Structures in Slowly Varying Media," Phys. D, **148**(1–2), pp. 49–96.

[7] Gallaire, F., Ruith, M., Meiburg, E., Chomaz, J.-M., and Huerre, P., 2006, "Spiral Vortex Breakdown as a Global Mode," J. Fluid Mech., **549**, pp. 71–80.

[8] Oberleithner, K., Sieber, M., Nayeri, C., Paschereit, C., Petz, C., Hege, H., Noack, B., and Wygnanski, I., 2011, "Three-Dimensional Coherent Structures in a Swirling Jet Undergoing Vortex Breakdown: Stability Analysis and Empirical Mode Construction," J. Fluid Mech., **679**(7), pp. 383–414.

[9] Oberleithner, K., Schimek, S., and Paschereit, C. O., 2015, "Shear Flow Instabilities in Swirl-Stabilized Combustors and Their Impact on the Amplitude Dependent Flame Response: A Linear Stability Analysis," Combust. Flame, **162**(1), pp. 86–99.

[10] Pierrehumbert, R. T., and Widnall, S. E., 1982, "The Two- and Three-Dimensional Instabilities of a Spatially Periodic Shear Layer," J. Fluid Mech., **114**, pp. 59–82.

[11] Barkley, D., 2006, "Linear Analysis of the Cylinder Wake Mean Flow," EPL (Europhys. Lett.), **75**(5), pp. 750–756.

[12] Fabre, D., Bonnefisa, P., Charru, F., Russo, S., Citro, V., Giannetti, F., and Luchini, P., 2014, "Application of Global Stability Approaches to Whistling Jets and Wind Instruments," International Symposium on Musical Acoustics (ISMA), Le Mans, France, July 7–12, pp. 23–28.

[13] Juniper, M. P., and Pier, B., 2015, "The Structural Sensitivity of Open Shear Flows Calculated With a Local Stability Analysis," Eur. J. Mech.-B/Fluids, **49**(Pt. B), pp. 426–437.

[14] Tammisola, O., and Juniper, M., 2016, "Coherent Structures in a Swirl Injector at Re = 4800 by Nonlinear Simulations and Linear Global Modes," J. Fluid Mech., **792**, pp. 620–657.

[15] Reynolds, W., and Hussain, A., 1972, "The Mechanics of an Organized Wave in Turbulent Shear Flow—Part 3: Theoretical Models and Comparisons With Experiments," J. Fluid Mech., **54**(2), pp. 263–288.

[16] Rukes, L., Paschereit, C. O., and Oberleithner, K., 2016, "An Assessment of Turbulence Models for Linear Hydrodynamic Stability Analysis of Strongly Swirling Jets," Eur. J. Mech.-B/Fluids, **59**, pp. 205–218.

[17] Ivanova, E. M., Noll, B. E., and Aigner, M., 2012, "A Numerical Study on the Turbulent Schmidt Numbers in a Jet in Crossflow," ASME J. Eng. Gas Turbines Power, **135**(1), p. 011505.

[18] Theofilis, V., 2011, "Global Linear Instability," Annu. Rev. Fluid Mech., **43**, pp. 319–352.

[19] Hecht, F., 2012, "New Development in FreeFem++," J. Numer. Math., **20**(3–4), pp. 251–265.

[20] Lehoucq, R., Sorensen, D., and Yang, C., 1997, *Arpack Users' Guide: Solution of Large Scale Eigenvalue Problems With Implicitly Restarted Arnoldi Methods*, SIAM, Philadelphia, PA.

[21] Paredes, P., Hermanns, M., Le Clainche, S., and Theofilis, V., 2013, "Order 10 4 Speedup in Global Linear Instability Analysis Using Matrix Formation," Comput. Methods Appl. Mech. Eng., **253**, pp. 287–304.

[22] Giannetti, F., and Luchini, P., 2007, "Structural Sensitivity of the First Instability of the Cylinder Wake," J. Fluid Mech., **581**, pp. 167–197.

[23] Orszag, S. A., 1971, "Accurate Solution of the Orr–Sommerfeld Stability Equation," J. Fluid Mech., **50**(4), pp. 689–703.

[24] Monkewitz, P. A., Huerre, P., and Chomaz, J.-M., 1993, "Global Linear Stability Analysis of Weakly Non-Parallel Shear Flows," J. Fluid Mech., **251**, pp. 1–20.

[25] Bers, A., 1983, "Space-Time Evolution of Plasma Instabilities-Absolute and Convective," Basic Plasma Phys., **1**, pp. 451–517.

[26] Briggs, R. J., 1964, "Electron-Stream Interaction With Plasmas," Science, **148**(3676), pp. 1453–1454.

[27] Poinsot, T., 2005, *The AVBP Handbook*, CERFACS, Toulouse, France.

[28] Colin, O., and Rudgyard, M., 2000, "Development of High-Order Taylor-Galerkin Schemes for LES," J. Comput. Phys., **162**(2), pp. 338 –371.

[29] Nicoud, F., Toda, H. B., Cabrit, O., Bose, S., and Lee, J., 2011, "Using Singular Values to Build a Subgrid-Scale Model for Large Eddy Simulations," Phys. Fluids, **23**(8), p. 085106.

[30] Schmid, P. J., 2010, "Dynamic Mode Decomposition of Numerical and Experimental Data," J. Fluid Mech., **656**, pp. 5–28.

[31] Juniper, M. P., Tammisola, O., and Lundell, F., 2011, "The Local and Global Stability of Confined Planar Wakes at Intermediate Reynolds Number," J. Fluid Mech., **686**, pp. 218–238.